Small Methods

small methods
www.small-methods.com

RESEARCH ARTICLE

Bio-Inspired Laccase-Mimicking Cu_3–MOF Nanozyme as Colorimetric Sensor Array for Rapid Degradation and Visual Sensing of Phenolic Compounds

Haitao Han[1] | YangCui Qu[1] | Xinhe Duan[2] | JunHao Cui[3] | Li Song[1] | Hao Wang[1] | Jie Yang[1] | Guannan Wang[2]

[1]College of Medical Engineering& the Key Laboratory for Medical Functional Nanomaterials Jining Medical University, Jining, Shandong, P. R. China | [2]School of Pharmacy, Shenyang Medical College, Shenyang, Liaoning, P. R. China | [3]Department of Orthopaedics, Shandong Provincial Hospital Affiliated to Shandong First Medical University, Jinan, Shandong, P. R. China

Correspondence: Guannan Wang (chemwangguannan@symc.edu.cn)

Received: 3 November 2025 | **Revised:** 19 December 2025 | **Accepted:** 21 December 2025

Keywords: chemical stability | colorimetric sensor array | nanozym | phenolics | trinuclear copper

ABSTRACT

Trinuclear copper complexes that emulate the active sites of multicopper oxidases (MCOs) are of broad biological interest. Here, a monoatomic-node strategy combined with solvent reduction was used to construct a rare trinuclear copper MOF featuring a planar, equilateral-triangular $Cu^{I}_{0.6}Cu^{II}_{2.4}$ core. The $Cu^{I}_{0.6}Cu^{II}_{2.4}$–MOF nanozyme shows enzymatic activity 37.2 times than that of laccase and 13.6 times than that of a Cu^{II}_{3}–MOF analogue, retains high chemical stability from pH 4 to 12, and lowers production cost by 16.2-fold relative to natural laccase. DFT calculations attribute the superior performance to the introduction of Cu^{+}, which yields a more favorable electronic structure, reaction energy landscape, and intermediate binding than in Cu^{II}_{3}–MOF. Consequently, $Cu^{I}_{0.6}Cu^{II}_{2.4}$–MOF efficiently degrades phenolic pollutants and enables colorimetric discrimination and detection of 11 phenols as a colorimetric sensor array. It also affords sensitive detection of epinephrine and dopamine, with limits of detection of 6.5 and 10 μM, respectively. Overall, this work demonstrates a laccase-inspired route to high-activity, low-cost MOFs with strong potential for environmental remediation and biosensing.

1 | Introduction

Trinuclear copper complexes have garnered significant attention due to their relevance in biological systems, particularly in enzymes like multicopper oxidases (MCOs), which catalyze crucial reactions such as the reduction of oxygen to water [1–4]. These enzymes, found in various organisms, are vital for the oxidative transformation of substrates and play central roles in several biochemical processes. Mimicking the structure and function of these natural systems has become a key goal in bioinorganic chemistry, offering the potential to develop efficient, non-precious metal catalysts for applications in biosensing, pharmaceutical diagnostics, therapy, and ecological monitoring [5–10].

Designing trinuclear copper catalysts that mimic oxidase enzymes presents significant challenges, primarily due to the need to position three copper ions at closely spaced distances (typically less than 5 Å), allowing simultaneous interaction with O_2 and the oxidizing substrate [11]. The repulsive forces between copper ions in solution complicate their close assembly during synthesis. Achieving such sub-5 Å Cu···Cu separations is technically demanding because strong electrostatic repulsion between Cu centers often prevents their stable assembly at

these short distances, and most organic ligands lack the rigid, preorganized geometry required to hold multiple metal ions in such constrained arrangements. Additionally, the catalyst must accommodate both Cu(I) and Cu(II) oxidation states, as these ions adopt different coordination geometries when bound to organic ligands, making it difficult to synthesize mimics containing both oxidation states [12, 13]. Moreover, constructing compounds with an odd number of metal ions adds further complexity [14]. These combined obstacles make the rational construction of a structurally well-defined, mixed-valence Cu_3 cluster particularly challenging, especially when attempting to control both metal–metal distances and electronic communication within the cluster. Several bioinspired materials have been reported to address these limitations. Wang et al. reported a Cys–His–Cu peptide-based nanozyme in which Cu^+/Cu^{2+} is coordinated by a dipeptide motif mimicking the T1 site and electron-transfer pathway of natural laccase [15]. However, the resulting structures lack well-defined multinuclear copper clusters. Similarly, GMP/Cu coordination assemblies stabilize Cu(II) through N-rich nucleoside ligands and exhibit laccase-like activity, yet they do not support the mixed-valence, spatially organized trinuclear arrangement required for multi-electron O_2 activation [16]. Porphyrinic MOFs and other MOF-based oxidase mimics possess rigid ligand frameworks resembling the aromatic environment of laccase, but they generally emulate only part of the laccase active site and do not reproduce the geometry of a closely spaced, mixed-valence Cu_3 cluster [17–19]. Therefore, selecting an appropriate synthetic strategy and designing ligands that stabilize the trinuclear copper arrangement at the correct distance while providing the necessary spatial organization for efficient catalysis are crucial for overcoming these challenges.

Various synthetic strategies have been developed to precisely control the number and arrangement of metal ions in metal–organic catalytic materials [20–24]. Among these, the monoatomic node synthesis approach has gained prominence as an effective method for regulating metal ion coordination within the material [25–27]. In this strategy, a metal ion serves as a central node to which organic ligands coordinate, forming a stable secondary building unit (SBU). To precisely construct the SBU and control the structure of the final product, the coordination sites of the ligand must meet the preferences of the metal ions. Rigid organic ligands with nitrogen-donating sites have proven effective for constructing polynuclear copper clusters [28–31]. For instance, Zhao and co-workers reported macrocycle-encircled polynuclear metal clusters, showing that rigid nitrogen-donor macrocycles preorganize coordination sites to match metal-ion preferences and template multi-metal assembly, enabling controllable formation of polynuclear copper clusters [32]. Chen et al. developed a Cu–MOF built from heptanuclear/binuclear Cu clusters and a rigid tetrazolyl–carboxylate ligand, resulting in a 3D anionic dodecahedral-cage framework [33]. Schneider et al. synthesized Cu(II) dimers, Cu(II) tetra-/hexanuclear clusters, and a mixed-valence Cu(I)/Cu(II) pentanuclear triple-decker, supported by polydentate pyridylamide ligands, with rigid N-donor geometries that preorganize Cu sites and direct SBU formation [34].

1H-pyrazole-4-carboxylic acid (H_2PyC), a small bifunctional ligand, features two N-donor sites at one end and a carboxylate group at the other. Its intraligand N···N distance of 1.36 Å promotes tight linkage of adjacent Cu ions. Each H_2PyC binds two Cu nodes via these donors, and repetition of this linkage assembles the SBU, while the carboxylate groups balance the charge to stabilize the framework. In this study, we employed a monoatomic-node strategy with the H_2PyC ligand to construct a rare trinuclear copper MOF featuring a planar, equilateral-triangular Cu_3 core (Scheme 1a). Using NMP as an electron-donating solvent partially reduces Cu(II) to Cu(I), producing copper oxidase mimics with both oxidation states, overcoming the challenge of synthesizing such mixed-state mimics (Scheme 1a). The resulting MOF- $Cu^{I}_{0.6}Cu^{II}_{2.4}$–MOF, with a particle size of 5 μm, was obtained by adjusting reaction time and temperature and serves as a model for mimicking the active sites of laccase (Scheme 1b). We evaluated the chemical stability of the synthesized material and compared its catalytic performance and stability to that of laccase. Theoretical calculations were also employed to investigate the catalytic mechanisms of the laccase mimic in both oxidation states. Finally, the $Cu^{I}_{0.6}Cu^{II}_{2.4}$–MOF was utilized as a laccase mimic for the degradation of phenolic pollutants and as an array sensor for detecting 11 phenolics (Scheme 1c). In biosensing applications, the $Cu^{I}_{0.6}Cu^{II}_{2.4}$–MOF demonstrated potential for detecting neurotransmitters such as dopamine (DA) and epinephrine (EP), with real sample tests highlighting its promising applicability in practical scenarios (Scheme 1d).

2 | Results and Discussion

2.1 | Structural Characterization of Cu^{II}_3–MOF and $Cu^{I}_{0.6}Cu^{II}_{2.4}$–MOF

The synthesized Cu^{II}_3–MOF forms octahedral blue crystals (Figure 1a) (detailed in the Supporting Information, Experimental Methods). Single-crystal diffraction revealed that Cu^{II}_3–MOF crystallizes in the tetragonal space group I41/acd (no. 142). As shown in Figure 1b, the asymmetric unit consists of one Cu atom, one H_2Pyc ligand, and one-third of a guest water molecule. Each Cu atom adopts a tetrahedral coordination, bonding with one O atom from a H_2Pyc ligand, two N atoms from different H_2Pyc ligands, and one coordinated water molecule (Figure 1c). Three Cu atoms coordinate to adjacent N atoms of H_2Pyc, forming a coplanar equilateral triangle (Cu1–Cu2–Cu3) with Cu···Cu distances of 3.4 Å (Figure 1d). The Cu···N distances range from 1.94 to 2.05 Å, and Cu···O distances range from 1.93 to 2.06 Å. The ∠N–Cu–N angles vary between 155.1° and 172.8°, while the ∠O–Cu–O angles range from 118.1° to 179.6°. Notably, Cu_3 shows a coordination environment similar to that of the trinuclear copper cluster in laccase (Figure 1e) [35–39]. The Cu_3 SBU is further bridged by six adjacent H_2Pyc ligands, forming a $[Cu_{21}]$ cluster node (Figure 1f). The dihedral angle between adjacent Cu_3 SBUs is 75.9°, and their dense connectivity induces strong steric hindrance, resulting in an almost perpendicular arrangement (Figure 1f). These Cu_3 SBUs link through neighboring $[Cu_{21}]$ nodes to form a layered architecture (Figure 1g). Within each $[Cu_{21}]$ node, two Cu_3 SBUs oriented nearly perpendicular to the plane connect to another Cu_3 SBU parallel to the plane in the adjacent layer (Figure 1g). This results in closely packed layers, forming a 3D network (Figure 1g). The Cu^{II}_3–MOF was synthesized using a method analogous to single-crystal synthesis by adjusting the reaction conditions. Scanning

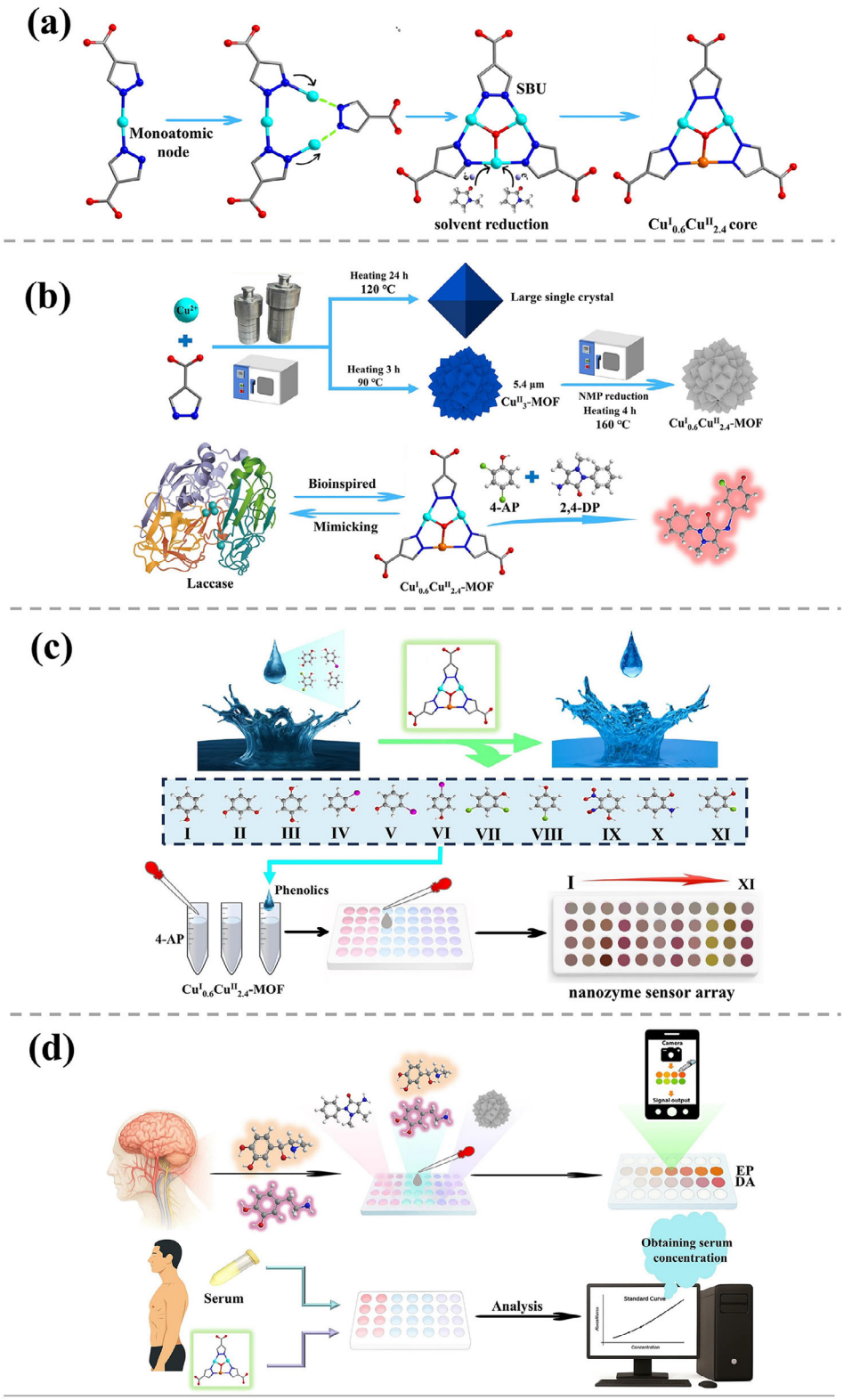

SCHEME 1 | Schematic of the (a) monoatomic-node strategy for synthesizing the trinuclear copper compound and solvent reduction synthesis for mixed-valence $Cu^{I}_{0.6}Cu^{II}_{2.4}$–MOF; (b) Synthesis process for the preparation of Cu–MOF crystal, Cu^{II}_{3}–MOF and $Cu^{I}_{0.6}Cu^{II}_{2.4}$–MOF nanozyme with laccase-mimicking copper center (4-AP= 4-aminoantipyrine; 2,4-DP=2,4-dichlorophenol); (c) $Cu^{I}_{0.6}Cu^{II}_{2.4}$–MOF nanozyme as a colorimetric sensor array for detection and oxidation of phenolic compounds; (d) Modules of Mobile Color Picker app for colorimetric detection of EP (epinephrine) and DA (dopamine) in real samples.

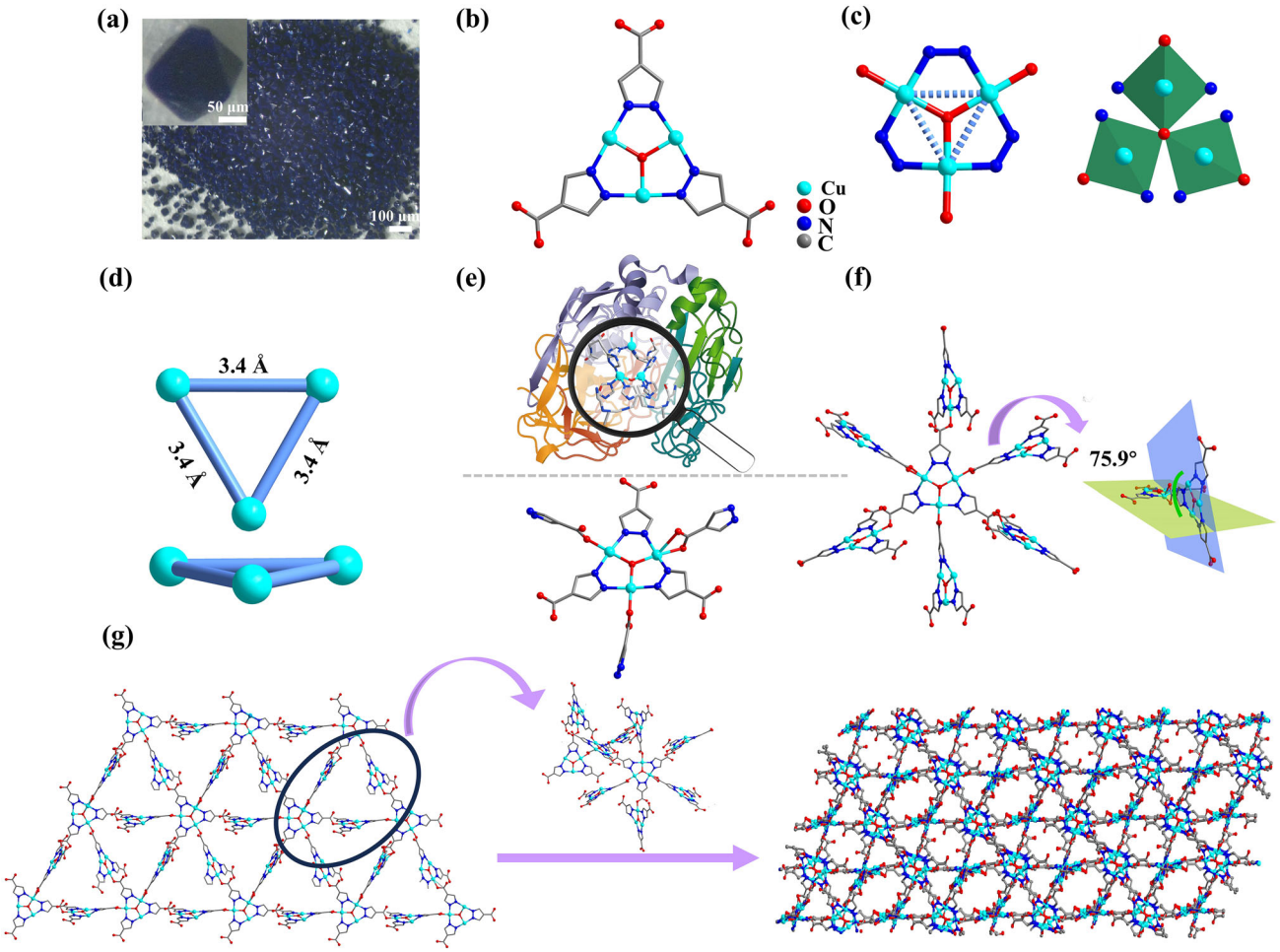

FIGURE 1 | (a) Single crystal image under optical microscope; (b) The SBU of Cu^{II}_3–MOF; (c) The coordinate environment and mode of Cu^{2+} ions; (d) A planar, equilateral-triangular Cu^{II}_3 core; (e) Schematic comparison of the Cu_3 core with laccase's trinuclear copper sites; (f) The dihedral angle between the planes of adjacent Cu_3 units; (g) formation of 3D Cu^{II}_3–MOF single crystal structure.

electron microscopy (SEM) analysis (Figure 2a–c) revealed that the Cu^{II}_3–MOF exhibited a coarse spherical morphology with sharp protrusions, averaging 5.4 μm in length. This unique morphology is likely a result of the self-assembly of the ligands and copper ions, along with the aggregation of crystal nuclei due to the shortened synthesis time. Energy-dispersive X-ray spectroscopy (EDX) was used to further characterize the Cu^{II}_3–MOF (Figure 2d–f), and elemental mapping confirmed the presence of Cu, O, and N. These results validated the successful formation of the Cu^{II}_3–MOF and showed a uniform distribution of Cu, N, and O elements. FT-IR spectroscopy was used to investigate the structural changes of H_2PyC and Cu^{II}_3–MOF. H_2PyC displayed a characteristic peak at 1695 cm^{-1}, corresponding to the C═O stretching vibration. The Cu^{II}_3–MOF exhibited peaks at 584, 1106, and 1645 cm^{-1}, which are assigned to Cu—O, Cu—N bonds, and C═O stretching vibration, respectively. Notably, the C═O stretching peak in the Cu^{II}_3–MOF shifted to a lower wavenumber compared to H_2PyC, likely due to the interaction between the carbonyl group and Cu^{2+} ions within the MOF structure (Figure S1). $Cu^{I}_{0.6}Cu^{II}_{2.4}$–MOF was synthesized by solvent reduction of Cu^{II}_3–MOF, as shown in Figure S2, where the color changes from blue to brown. SEM analysis indicated that the morphology and elemental distribution of $Cu^{I}_{0.6}Cu^{II}_{2.4}$–MOF remained consistent, suggesting that the solvent reduction process did not alter the material's structure or morphology (Figure 2g–l). X-ray photoelectron spectroscopy (XPS) analysis confirmed the presence of Cu, O, N, and C elements in Cu^{II}_3–MOF (Figure S3a). The high-resolution Cu 2p XPS spectrum of Cu^{II}_3–MOF showed peaks corresponding to the Cu $2p_1/_2$ and Cu $2p_3/_2$ binding energies of Cu^{2+} at 952.98 and 933.14 eV, respectively (Figure S3b). In contrast, the high-resolution Cu 2p XPS spectrum of $Cu^{I}_{0.6}Cu^{II}_{2.4}$–MOF displayed peaks for Cu^{2+} at 953.89 and 934.07 eV, along with peaks for Cu^{+}/Cu^{0} at 952.24 and 932.71 eV (Figure 2m). The Cu LMM Auger peaks of $Cu^{I}_{0.6}Cu^{II}_{2.4}$–MOF -MOF at 915.76 eV further confirmed the presence of Cu^{+} (Figure 2n). Based on the peak areas, 97.06% of the copper in $Cu^{I}_{0.6}Cu^{II}_{2.4}$–MOF remains as Cu^{2+}, while 20.94% exists as Cu^{+} (Figure 2o). TG analysis shows that Cu^{II}_3–MOF undergoes a significant weight loss from room temperature to about 112°C, attributed to the removal of guest solvents. A more substantial and continuous weight-loss process occurs between 166°C and 344°C, corresponding to the release of coordinated solvent molecules and the partial decomposition of the organic framework. Significant framework degradation begins around 344°C, and the material stabilizes near 800°C (Figure S4a). In contrast, $Cu^{I}_{0.6}Cu^{II}_{2.4}$–MOF shows negligible weight loss from room temperature to about 140°C, indicating fewer guest molecules in $Cu^{I}_{0.6}Cu^{II}_{2.4}$–MOF in the low-temperature region. A sharp weight-loss step between 140°C

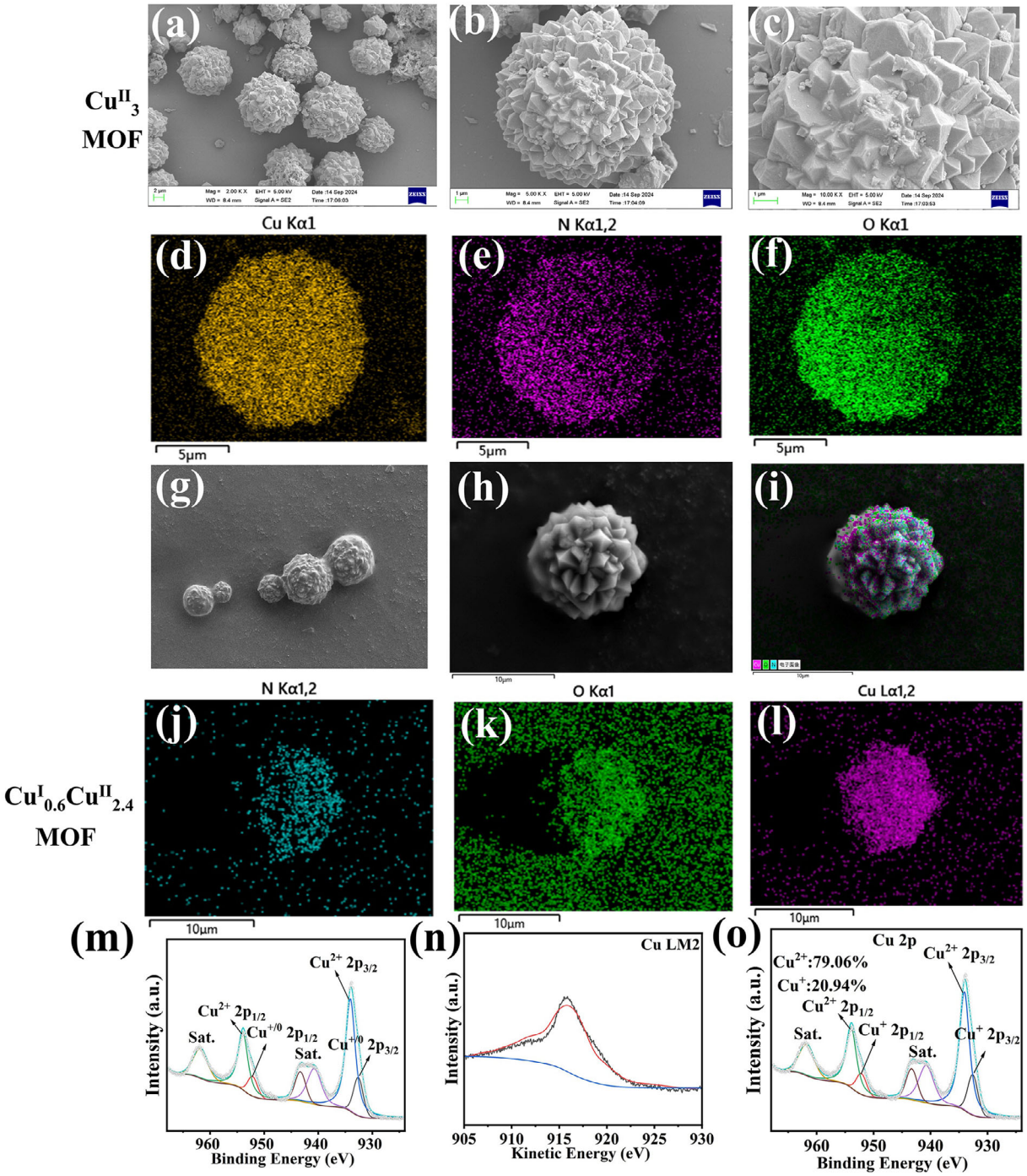

FIGURE 2 | (a–c) SEM images and (d–f) elemental mappings of Cu^{II}_3–MOF; (g–i) SEM images and (j–l) elemental mappings of $Cu^{I}_{0.6}Cu^{II}_{2.4}$–MOF (m) Cu 2p XPS spectrum of $Cu^{I}_{0.6}Cu^{II}_{2.4}$–MOF; (n–o) Cu 2p and Cu LMM Auger XPS spectra of $Cu^{I}_{0.6}Cu^{II}_{2.4}$–MOF.

and 390°C is associated with the removal of coordinated solvents and the main framework decomposition. Above 390°C, the mass decreases gradually until stabilization near 800°C (Figure S4b).

2.2 | Characterization of Cu^{II}_3–MOF and $Cu^{I}_{0.6}Cu^{II}_{2.4}$–MOF

The chemical stability of Cu^{II}_3–MOF and $Cu^{I}_{0.6}Cu^{II}_{2.4}$–MOF was assessed in solutions with pH values ranging from 4 to 12. The experimentally obtained PXRD patterns were consistent with the simulated patterns, confirming the excellent chemical stability of both Cu^{II}_3–MOF and $Cu^{I}_{0.6}Cu^{II}_{2.4}$–MOF (Figures S5–S7). Next, the laccase-like activities of Cu^{II}_3–MOF, $Cu^{I}_{0.6}Cu^{II}_{2.4}$–MOF, and laccase were evaluated through the reaction between 4-aminoantipyrine (4-AP), 2,4-dichlorophenol (2,4-DP). When the above MOFs and laccase introduced into a mixed solution of 2,4-DP and 4-AP, a distinct red color develops. This color change originates from an oxidative coupling process catalyzed by the trinuclear copper centers within the MOFs or by the active sites of natural laccase. In this process, the catalysts promote the oxidation of 2,4-DP to generate phenoxy radicals, which subsequently

couple with 4-AP to form a quinone-imine chromophore. This species exhibits strong absorption in the visible region and is responsible for the observed red color (Figure 3a). Under identical conditions, the catalytic performance of $Cu^{I}_{0.6}Cu^{II}_{2.4}$–MOF was approximately 13.6 times higher than that of Cu^{II}_{3}–MOF and 37.2 times higher than that of natural laccase (Figure 3b). Additionally, the catalytic activities of $Cu^{I}_{0.6}Cu^{II}_{2.4}$–MOF and laccase were evaluated in Tri-HCl and MES buffer solutions. $Cu^{I}_{0.6}Cu^{II}_{2.4}$–MOF exhibited significantly higher activity than laccase in both buffers, with catalytic activity approximately 60 times and 2.6 times greater than that of laccase in Tri-HCl and MES, respectively (Figure S8). Notably, $Cu^{I}_{0.6}Cu^{II}_{2.4}$–MOF exhibited the highest activity in PBS buffer solution. These results demonstrate that $Cu^{I}_{0.6}Cu^{II}_{2.4}$–MOF shows significantly enhanced laccase-like activity compared to both Cu^{II}_{3}–MOF and natural laccase.

The kinetic parameters of the $Cu^{I}_{0.6}Cu^{II}_{2.4}$–MOF were determined using the Michaelis–Menten equation (Figure 3c), with the K_m and V_m values summarized in Table S2. The K_m value of $Cu^{I}_{0.6}Cu^{II}_{2.4}$–MOF is 3.59×10^{-3} mM·min^{-1}, and the V_m value is 0.26 mM (Figure 3d). The K_m value is lower than that of some other Cu–MOF mimics [15, 40], indicating its excellent substrate affinity. Additionally, a comparison of the V_m value with those reported in other studies (Table S2) suggests that $Cu^{I}_{0.6}Cu^{II}_{2.4}$–MOF exhibits a similar microstructure to natural laccase, which likely enhances its electron transfer rate and overall activity. The catalytic performance of $Cu^{I}_{0.6}Cu^{II}_{2.4}$–MOF and natural laccase was assessed under various pH conditions (Figure 3e). Natural laccase activity sharply decreased and became inactive at pH > 9, while $Cu^{I}_{0.6}Cu^{II}_{2.4}$–MOF maintained higher activity at pH 11 than at pH 7. This demonstrates the ability of $Cu^{I}_{0.6}Cu^{II}_{2.4}$–MOF to perform catalysis in harsh alkaline conditions. Various factors influencing catalytic performance were systematically analyzed. First, the impact of NaCl was explored (Figure 3f). As NaCl concentration increased, natural laccase activity sharply declined, likely due to Cl^- ions acting as inhibitors. In contrast, the catalytic activity of $Cu^{I}_{0.6}Cu^{II}_{2.4}$–MOF increased significantly with rising NaCl concentrations, showing a 2.5-fold enhancement at 0.5 mol/L NaCl. This improvement is attributed to the facilitation of substrate adsorption on the $Cu^{I}_{0.6}Cu^{II}_{2.4}$–MOF surface by NaCl, consistent with trends observed in previous studies [15, 41, 42]. The effect of temperature on catalytic performance was also examined (Figure 3g). While the catalytic activity of natural laccase declined with increasing temperature (40°C to 90°C), $Cu^{I}_{0.6}Cu^{II}_{2.4}$–MOF maintained stable activity across a broad temperature range of 30°C to 90°C. Even after incubation at 90°C for 30 min, $Cu^{I}_{0.6}Cu^{II}_{2.4}$–MOF retained over 80% of its activity, demonstrating its exceptional thermal stability. Ethanol presence negatively impacted catalytic performance (Figure 3h), and both laccase and $Cu^{I}_{0.6}Cu^{II}_{2.4}$–MOF showed decreased activity at higher ethanol concentrations, likely due to ethanol inhibiting the reaction process. The stability of $Cu^{I}_{0.6}Cu^{II}_{2.4}$–MOF and laccase was assessed after storage at ambient temperature (Figure 3i). While laccase activity steadily declined over seven days, $Cu^{I}_{0.6}Cu^{II}_{2.4}$–MOF retained over 90% of its catalytic efficiency, highlighting its superior storage stability. The recyclability of $Cu^{I}_{0.6}Cu^{II}_{2.4}$–MOF was also evaluated as a key factor for practical applications (Figure 3j). After six cycles, $Cu^{I}_{0.6}Cu^{II}_{2.4}$–MOF retained approximately 80% of its catalytic activity, indicating excellent reusability. In addition, XRD analysis, SEM morphology, and elemental mapping of the recovered $Cu^{I}_{0.6}Cu^{II}_{2.4}$–MOF confirm the preservation of its structural integrity, demonstrating its stable catalytic performance during repeated use (Figures S9 and S10). XPS analysis revealed changes in the oxidation state of copper after catalysis (Figure S11). The results show a shift in the binding energy of Cu^+, indicating that Cu^+ ions participated in the catalytic process. These results demonstrate that $Cu^{I}_{0.6}Cu^{II}_{2.4}$–MOF outperforms natural laccase in catalytic stability, thermal resistance, and storage durability. Additionally, $Cu^{I}_{0.6}Cu^{II}_{2.4}$–MOF is 16.2 times cheaper to produce than an equivalent weight of natural laccase (Table S3), highlighting its significant cost advantage. The ability of $Cu^{I}_{0.6}Cu^{II}_{2.4}$–MOF to maintain high activity under challenging conditions, combined with its recyclability and low production costs, makes it a highly promising candidate for practical catalytic applications.

2.3 | Catalytic Degradation of Phenolic Pollutants of $Cu^{I}_{0.6}Cu^{II}_{2.4}$–MOF

Phenolic compounds are toxic environmental pollutants, making their oxidation and degradation essential for environmental protection. To evaluate this, $Cu^{I}_{0.6}Cu^{II}_{2.4}$–MOF was incubated with phenolic compounds 2,4-DP, phenol (P), hydroquinone (HQ), 4-iodophenol (4-IP), and the chromogenic agent 4-AP. As shown in Figure 3k, $Cu^{I}_{0.6}Cu^{II}_{2.4}$–MOF effectively catalyzed the oxidation of these phenolic compounds, with the highest catalytic efficiency observed for 2,4-DP, followed by P, 4-IP, and HQ. This highlights $Cu^{I}_{0.6}Cu^{II}_{2.4}$–MOF as a viable alternative to natural enzymes for treating phenolic compounds. To further assess its performance in high-salinity and high-pH environments, the catalytic activity of $Cu^{I}_{0.6}Cu^{II}_{2.4}$–MOF was compared with that of three previously reported Cu–MOF materials (Cu-TCPP, Cu-HKUST, and Cu-BDC) (Figures S12–S14) [43–45]. When the four Cu–MOFs were soaked in 0.1, 0.5, and 1 M NaCl solutions, the catalytic activity of Cu-HKUST, Cu-BDC, and $Cu^{I}_{0.6}Cu^{II}_{2.4}$–MOF increased with the concentration of NaCl. In contrast, the activity of Cu-TCPP showed little change. Notably, $Cu^{I}_{0.6}Cu^{II}_{2.4}$–MOF demonstrated significantly higher catalytic activity than the other three Cu–MOFs across all NaCl concentrations (Figure 3l). Furthermore, $Cu^{I}_{0.6}Cu^{II}_{2.4}$–MOF outperformed the other three Cu–MOFs in a pH 11 solution (Figure 3m). These results underscore the superior performance of $Cu^{I}_{0.6}Cu^{II}_{2.4}$–MOF as a nanozyme catalyst for the degradation of phenolic compounds in high-salinity and high-pH wastewater.

2.4 | Construction of Colorimetric Sensor Array for the Discrimination of Phenolic Pollutants

The varying biological toxicity and environmental impact of different phenolic pollutants underscore the urgent need for a simple strategy to distinguish these compounds. However, simultaneous detection of multiple phenolic compounds remains challenging due to their similar structures and reactivity, which complicates differentiation with a single sensor. $Cu^{I}_{0.6}Cu^{II}_{2.4}$–MOF/4-AP offers a solution, as phenolic compounds react with it to produce distinct color changes that intensify with increasing substrate concentration. Image feature information is extracted from the colorimetric visualizations of these phenolic pollutants (Figure 4a). This dataset—comprising image features, associated

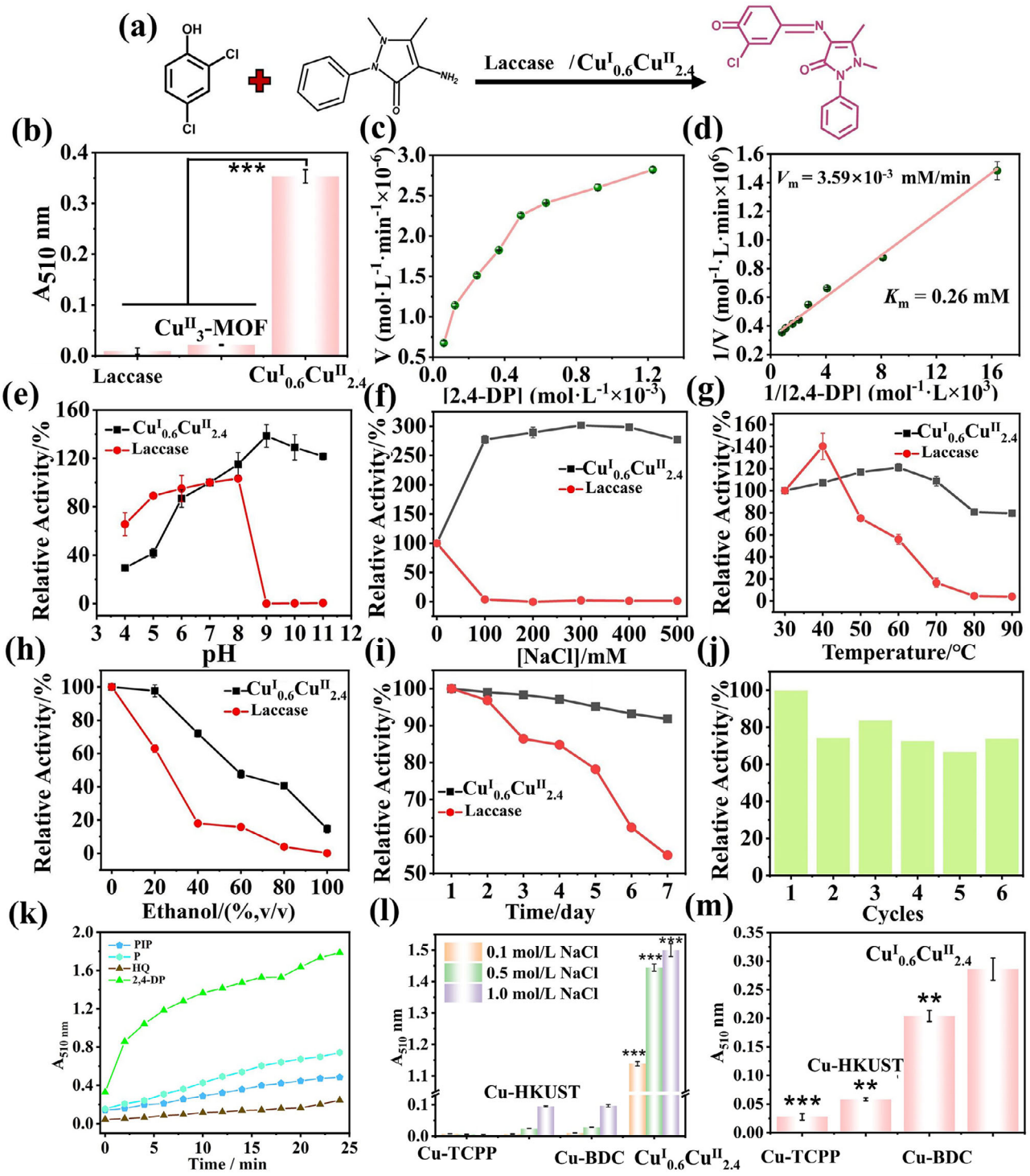

FIGURE 3 | (a) Cu$^{II}_{3}$–MOF, Cu$^{I}_{0.6}$Cu$^{II}_{2.4}$–MOF or laccase as catalysts for the reaction of 2,4-DP and 4-AP; (b) Catalytic activity of Cu$^{II}_{3}$–MOF, Cu$^{I}_{0.6}$Cu$^{II}_{2.4}$–MOF and laccase determined by monitoring UV–vis absorption at 510 nm in PBS solution (pH 7, 0.1 mol/L); (c) Dependence of reaction rate on 2,4-DP concentration; (d) Lineweaver-Burk plot for reaction between 2,4-DP and 4-AP catalyzed by catalyzed by Cu$^{I}_{0.6}$Cu$^{II}_{2.4}$–MOF. Catalytic activities of Cu$^{I}_{0.6}$Cu$^{II}_{2.4}$–MOF and natural laccase at identical mass concentrations with varying (e) pH value, (f) salinity, (g) temperature, (h) ethanol concentration, (i) storage duration, and (j) cycle number; (k) Catalytic activity of Cu$^{I}_{0.6}$Cu$^{II}_{2.4}$–MOF toward different phenolics mixed with 4-AP for 24 min, as determined by absorbance at 510 nm; (l) UV–vis absorption spectra of 2,4-DP and 4-AP catalyzed by four different Cu–MOFs or Cu$^{I}_{0.6}$Cu$^{II}_{2.4}$–MOF in 0.1, 0.5, 1 M NaCl solution, respectively (***$p < 0.001$, compared to the other three groups at the same NaCl concentration). (m) UV–vis absorption spectra of 2,4-DP and 4-AP catalyzed by four different Cu–MOFs or Cu$^{I}_{0.6}$Cu$^{II}_{2.4}$–MOF in pH 11 solution (**$p < 0.01$, ***$p < 0.001$, all compared to the Cu$^{I}_{0.6}$Cu$^{II}_{2.4}$–MOF group). All quantitative data are presented as mean ± standard deviation (SD) from three independent experiments ($n = 3$, **$p <$ 0.01, ***$p < 0.001$). Kinetic parameters were obtained by nonlinear fitting of the Michaelis–Menten equation. No statistical significance testing was applied unless otherwise stated.

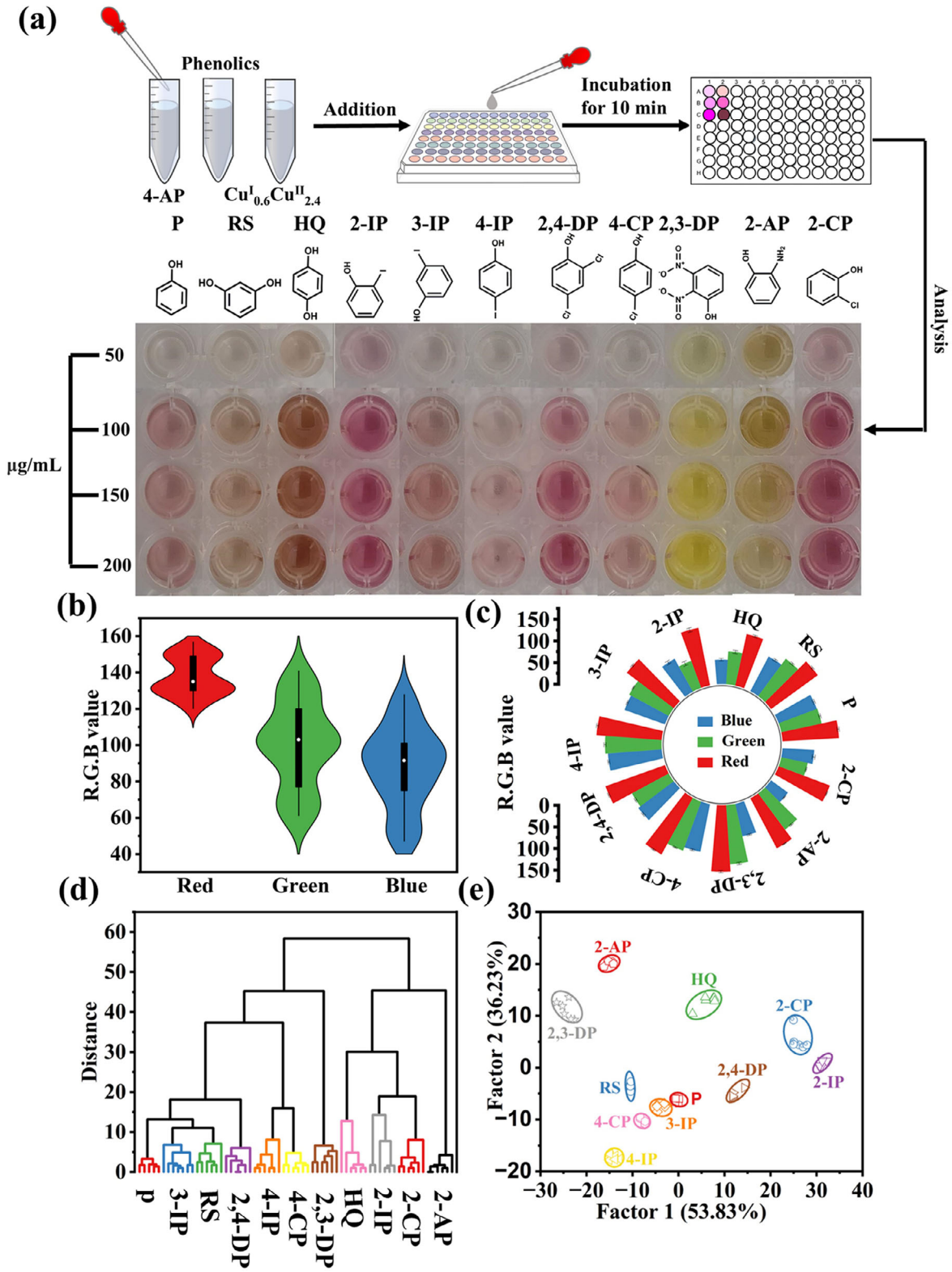

FIGURE 4 | (a) The chemical structure of 11 types of phenolic compounds and the concentration-dependent color change of them. Condition: 0.2 mg/mL $Cu^{I}_{0.6}Cu^{II}_{2.4}$–MOF, 50–200 mg/mL substrates, 0.25 mg/mL 4-AP, 0.1 mol/L PBS buffer, pH 7.0; (b) Violin plots of the distribution of corimetric response patterns characterization data for phenolics; (c) Distinct signal responses of features to 11 phenolics; (d) HCA-based classification of 11 phenolics using Red, Green, and Blue (RGB) image feature responses; (e) Linear discriminant analysis (LDA) canonical score plot from the corimetric response pattern. The scores were generated through LDA with 95% confidence ellipses. RGB values were extracted from digital images using ImageJ software. HCA was performed using Origin 2022 software (Origin 2022 Learning Edition), and LDA was carried out using classical LDA in SYSTAT (version 13.0). All colorimetric measurements were performed in six independent experiments ($n = 6$), and the six sets of RGB values were used for multivariate analysis.

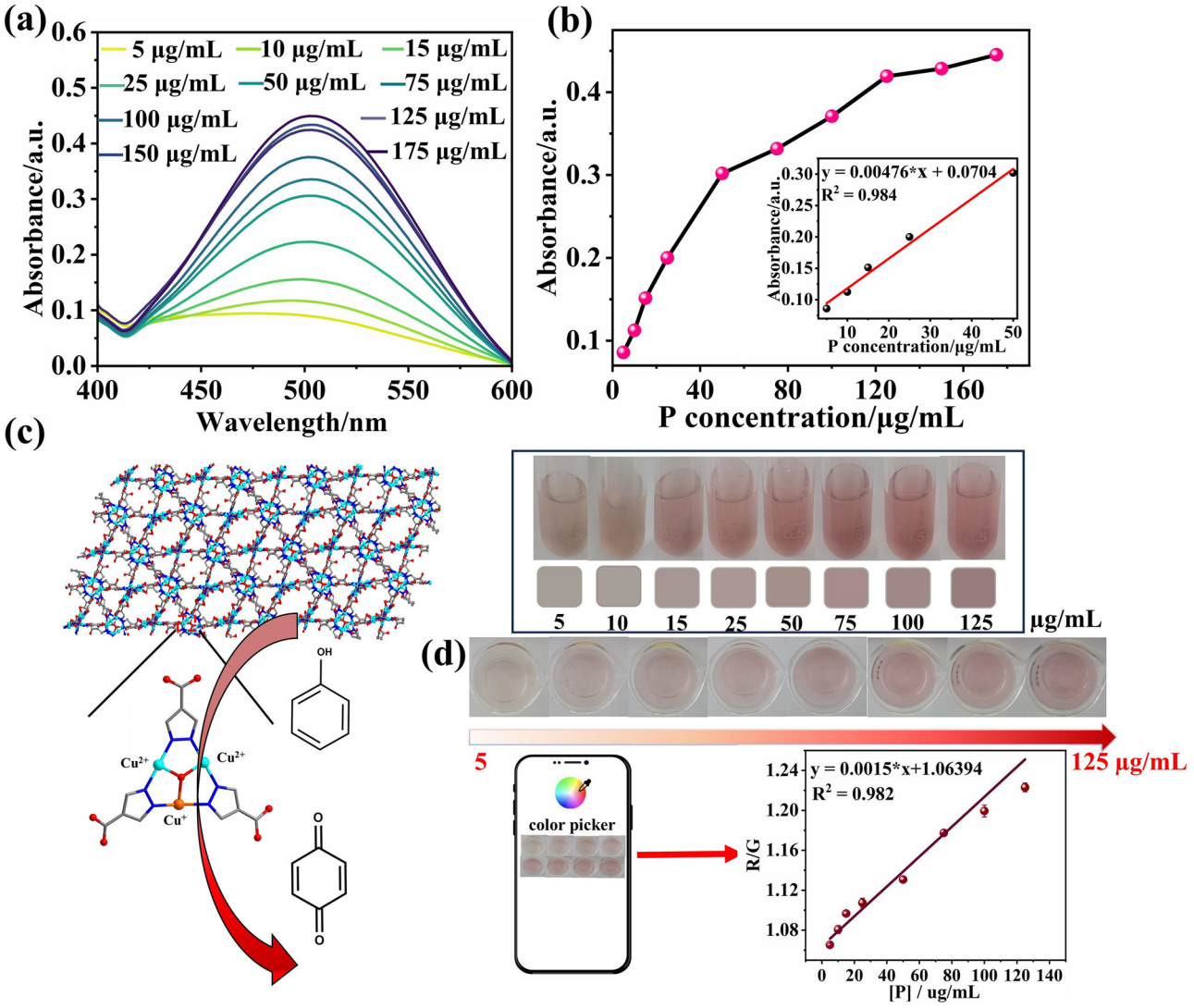

FIGURE 5 | (a) Absorbance of 5–175 μg/mL of P catalyzed by $Cu^{I}_{0.6}Cu^{II}_{2.4}$–MOF for 10 min. (b) Fitting curve of 5–50 μg/mL of P in the presence of $Cu^{I}_{0.6}Cu^{II}_{2.4}$–MOF (inset: linear calibration plot for different concentrations of P in the reaction system). (c) Naked-eye rapid detection of P catalyzed by $Cu^{I}_{0.6}Cu^{II}_{2.4}$–MOF based on colorimetric signal. (d) RGB values (R/G) obtained from smartphone images utilized for the precise detection of P in Mobile Color Picker app of smartphone. Data are presented as mean ±SD ($n = 3$).

phenolic compounds, and category labels—forms the training set. To better understand the data distribution, a violin plot of the original data was generated (Figure 4b). The plot reveals that the Red feature data is compact, while the Blue and Green features show a wider range of variability, highlighting the significant responsiveness of the Red feature in this study. Radial bar charts, derived from these statistics, visually represent feature variations across different phenolic compounds. Each feature displayed distinct signal responses to the 11 phenolic compounds (Figure 4c). The RGB (Red, Green, Blue) image feature response patterns were transformed into Euclidean distances using a hierarchical clustering algorithm (HCA), which successfully classified all 11 phenolic compounds with no misclassifications. This demonstrates the array's robust ability to differentiate between various types of phenolic compounds (Figure 4d). To further enhance the sensor array's ability to discriminate among the 11 phenolic compounds and predict unknown samples, machine learning algorithms were employed. A visual discrimination model was implemented using the Linear Discriminant Analysis (LDA) algorithm. The training matrix (3 features × 11 phenolic compounds × 6 replicates) was processed through the LDA algorithm to produce typical scores. In the LDA plot, each factor represents its contribution to the overall categorization. The first discriminant factor (factor 1), which provided the best discrimination among the classes, while factor 2 comprises the second highest degree of variance. Factor 1 and Factor 2 accounting for 58.83% and 36.23% of the variance, respectively. The 11 phenolic compounds were clearly categorized into six distinct groups (Figure 4e), with no misclassifications, achieving 100% discrimination accuracy. All of the 44 unknown phenolic compounds were correctly identified, representing an accuracy of 100%.

Phenol (P) is a significant organic compound found in various sources, and it is widely recognized for its negative environmental impact, particularly in water systems. This study investigates the use of $Cu^{I}_{0.6}Cu^{II}_{2.4}$–MOF as a sensing agent for the detection of P. In the presence of $Cu^{I}_{0.6}Cu^{II}_{2.4}$–MOF, P concentrations were

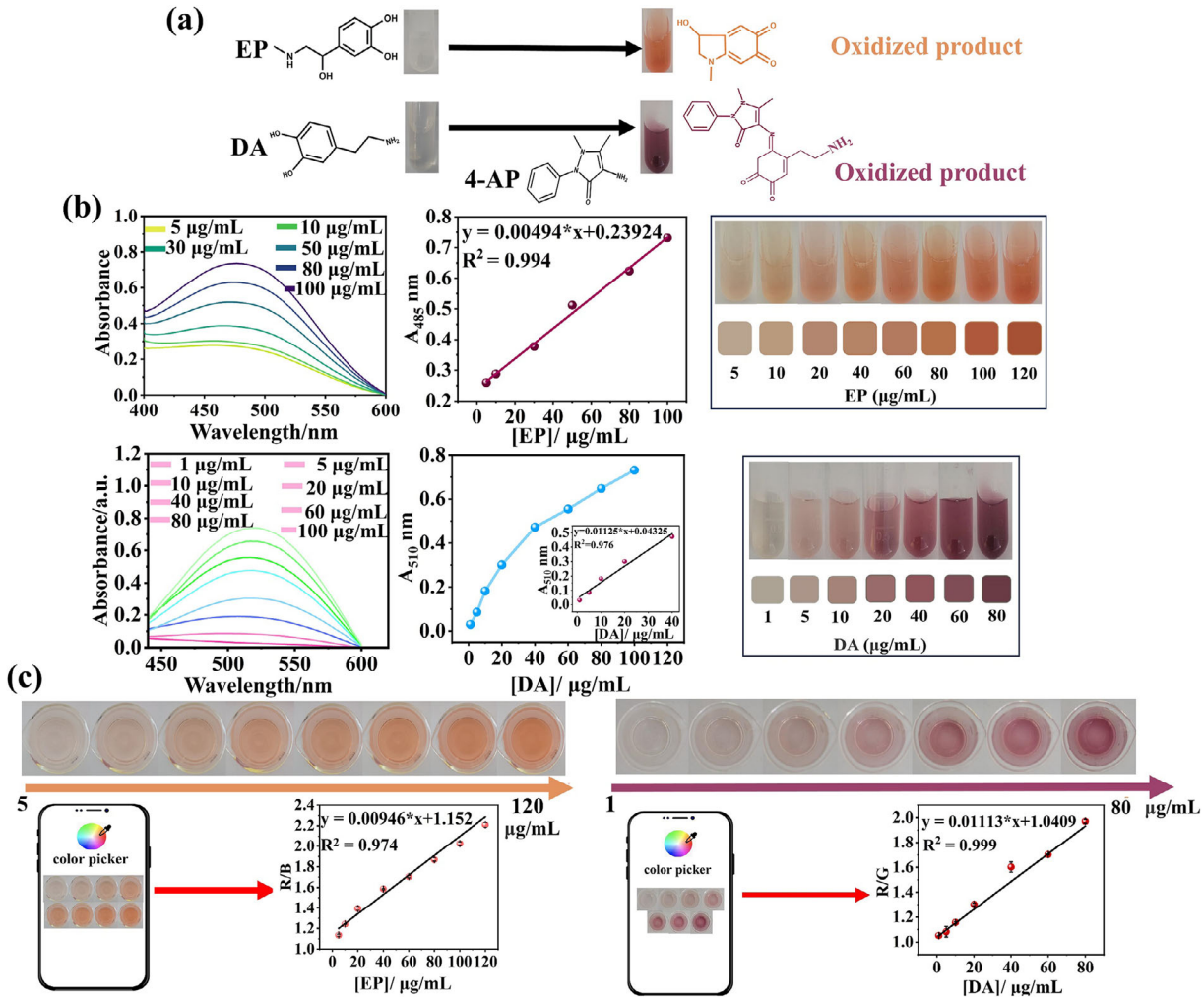

FIGURE 6 | (a) Laccase-mimicking $Cu^{I}_{0.6}Cu^{II}_{2.4}$–MOF and its application to detect EP and DA; (b) Absorbance of EP and DA, and fitting curve of various concentrations of EP and DA based on absorbance at 485 and 510 nm, respectively, with colorimetric cards catalyzed by $Cu^{I}_{0.6}Cu^{II}_{2.4}$–MOF; (c) Modules of Mobile Color Picker app for colorimetric detection of EP and DA detection. Data are presented as mean ±SD ($n = 3$).

quantified by measuring the absorbance at 510 nm, within a concentration range of 5–50 μg/mL (Figure 5a). The limit of detection (LOD) for phenol was calculated using the formula 3σ/slope (where σ represents the standard deviation of five blank samples), and was found to be 0.82 μg/mL (8.72 μM) (Figure 5b). Notably, the color of the phenol solution changed to red within 10 min (Figure 5c). Furthermore, a smartphone-based detection platform was developed to monitor phenol concentrations in aquatic environments. When phenol solutions were monitored in real-time using a smartphone camera, the RGB values (R/G) derived from the images were strongly correlated with phenol concentration (Figure 5d). The LOD for phenol detection using RGB values was determined to be 2.34 μg/mL (24.87 μM). The selectivity of $Cu^{I}_{0.6}Cu^{II}_{2.4}$–MOF for P detection was further evaluated in the presence of potential interferents, including $CaCl_2$, NaCl, $MgCl_2$, $NaNO_3$, and Na_2SO_4. The concentration of P was set at 100 μg/mL, and the interferents were tested at 200 μg/mL. As shown in Figure S15, significant absorbance was observed at 510 nm only for P. In the presence of these interferents, the absorbance at 510 nm was negligible, demonstrating the high selectivity of $Cu^{I}_{0.6}Cu^{II}_{2.4}$–MOF for P detection. In comparison to other sensors listed in Table S4, $Cu^{I}_{0.6}Cu^{II}_{2.4}$–MOF demonstrated comparable detection performance. Therefore, this $Cu^{I}_{0.6}Cu^{II}_{2.4}$–MOF-based colorimetric platform offers a rapid and effective method for detecting phenol in water, providing valuable support for environmental monitoring and pollution assessment.

2.5 | Rapid Detection of Epinephrine and Dopamine

Epinephrine (EP) and dopamine (DA) are important neurotransmitters and hormones that help the body respond to stress. The rapid and accurate detection of EP and DA is crucial for diagnosing conditions such as adrenal tumors and allergic reactions. Due to its laccase-like activity, $Cu^{I}_{0.6}Cu^{II}_{2.4}$–MOF can oxidize EP and DA in the presence of 4-AP, forming colored oxidation products (Figure 6a). The potential of $Cu^{I}_{0.6}Cu^{II}_{2.4}$–MOF for colorimetric detection of EP and DA was evaluated by adding the nanozyme to EP solutions (5–100 μg/mL) and DA solutions (1–100 μg/mL) for 10 min. The absorbance of the oxidized products was measured at 485 nm for EP and 510 nm for DA (Figure 6b). As the concentrations of EP and DA

increased, absorbance gradually increased. Calibration curves were plotted for both EP and DA detection, with detection limits of 0.79 μg/mL (4.32 μM) for EP and 0.35 μg/mL (2.28 μM) for DA. These results confirm the effectiveness of $Cu^{I}_{0.6}Cu^{II}_{2.4}$–MOF for the rapid detection of EP and DA. Moreover, compared to other nanozymes listed in Tables S5 and S6, $Cu^{I}_{0.6}Cu^{II}_{2.4}$–MOF demonstrated a wider detection range, shorter incubation time, and comparable detection performance for EP, as well as a shorter incubation time and comparable detection performance for DA.

Two colorimetric cards were developed for the quantitative detection of EP and DA concentrations using $Cu^{I}_{0.6}Cu^{II}_{2.4}$–MOF, as shown in Figure 6b. These cards allow for visual and semi-quantitative analysis of EP and DA concentrations, providing a colorimetric response with a gradient of intensities corresponding to EP concentrations from 5 to 120 μg/mL and DA concentrations from 1 to 80 μg/mL. Additionally, two rapid detection platforms were created by integrating a smartphone with the colorimetric reaction. These platforms have detection limits of 2.13 μg/mL (11.64 μM) for EP and 2.47 μg/mL (13.9 μM) for DA, enabling portable measurement of EP and DA concentrations (Figure 6c). The practical application of $Cu^{I}_{0.6}Cu^{II}_{2.4}$–MOF was further assessed through control experiments to evaluate its selectivity in the presence of interferents such as $CaCl_2$, cysteine, glutathione, glucose, lactose, and ascorbic acid. The analyte concentrations were 50 μg/mL for EP and 30 μg/mL for DA. As shown in Figures S16 and S17, only EP and DA catalysis resulted in significant absorbance at 485 and 510 nm, respectively. In the presence of the interfering agents, absorbance at 485 nm (for EP detection) and 510 nm (for DA detection) was negligible, demonstrating the high selectivity of $Cu^{I}_{0.6}Cu^{II}_{2.4}$–MOF for EP and DA detection. $Cu^{I}_{0.6}Cu^{II}_{2.4}$–MOF exhibits high selectivity for EP and DA due to its laccase-like oxidation mechanism, which preferentially catalyzes substrates containing phenolic hydroxyl groups. Both EP and DA possess an ortho-di-hydroxy structure, allowing them to be efficiently oxidized by the Cu(I)/Cu(II) redox centers in the MOF. The oxidation of EP by the Cu(I)/Cu(II) centers leads to significant color changes, while the oxidation product of DA reacts with 4-AP to form a red-colored compound. In contrast, interferents such as cysteine, glucose, and ascorbic acid lack the necessary di-hydroxy structure and do not undergo efficient oxidation under the mild catalytic conditions of $Cu^{I}_{0.6}Cu^{II}_{2.4}$–MOF, resulting in negligible absorbance changes (Figures S18 and S19). Finally, the practical application of these sensors was evaluated for detecting EP and DA in human blood serum samples (experimental details are provided in the methods section). To assess the accuracy of the method, recovery rates of standard EP and DA spiked into diluted serum samples were determined. The recovery rates for EP ranged from 91.26% to 102.1%, and for DA, from 102.9% to 117.0%, as summarized in Tables S7 and S8. These results demonstrate that the prepared sensor is effective for reliably determining EP and DA concentrations in real biological samples.

2.6 | Catalytic Mechanism of $Cu^{I}_{0.6}Cu^{II}_{2.4}$–MOF and Cu^{II}_{3}–MOF

Building on structural and performance analyses of $Cu^{I}_{0.6}Cu^{II}_{2.4}$–MOF and Cu^{II}_{3}–MOF, together with prior reports on laccase catalysis [46–48], we propose the catalytic pathway for 2,4-DP (Figures S20 and S21). For Cu^{II}_{3}–MOF, the cycle comprises four steps-substrate trapping, substrate oxidation, O_2 binding, and O_2 reduction to H_2O-whereas $Cu^{I}_{0.6}Cu^{II}_{2.4}$–MOF proceeds through five steps by adding an electron-transfer step. Consistent with experiments, $Cu^{I}_{0.6}Cu^{II}_{2.4}$–MOF shows markedly higher activity. DFT calculations rationalize this enhancement: the Cu^{+}-containing $Cu^{I}_{0.6}Cu^{II}_{2.4}$–MOF has a lower lowest unoccupied molecular orbital (LUMO) level (−2.71 eV vs −2.44 eV) and a higher highest occupied molecular orbital (HOMO) level (−6.35 eV vs −7.08 eV) than Cu^{II}_{3}–MOF, facilitating electron acceptance as well as excitation/transfer (Figure 7a). Differential charge-density analyses confirm stronger, more balanced interactions between $Cu^{I}_{0.6}Cu^{II}_{2.4}$–MOF and O_2-derived intermediates, stabilizing critical species (Figure 7a). Free-energy profiles further show lower barriers for $Cu^{I}_{0.6}Cu^{II}_{2.4}$–MOF at all key steps, with pronounced stabilization at the *OOH and *O stages,

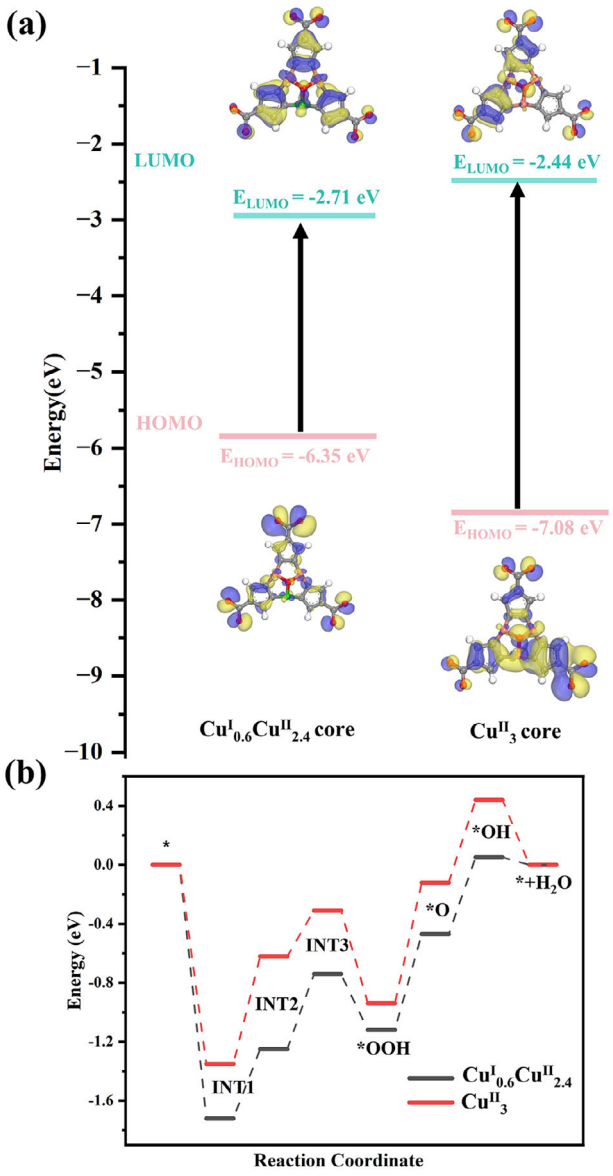

FIGURE 7 | (a) Electron density distributions on the HOMO and LUMO energy levels of $Cu^{I}_{0.6}Cu^{II}_{2.4}$–MOF and Cu^{II}_{3}–MOF and (b) free energy diagram in the laccase-mimicking process.

indicating superior kinetics (Figure 7b). Overall, by introducing Cu^{+}, $Cu^{I}_{0.6}Cu^{II}_{2.4}$–MOF attains a more favorable electronic structure, energy landscape, and intermediate binding than Cu^{II}_{3}–MOF, thereby delivering superior catalytic performance.

3 | Conclusion

A rare trinuclear copper MOF with a planar, equilateral-triangular $Cu^{I}_{0.6}Cu^{II}_{2.4}$ core was constructed via a monoatomic-node strategy coupled with solvent reduction, emulating the active-site architecture of multicopper oxidases. $Cu^{I}_{0.6}Cu^{II}_{2.4}$–MOF shows laccase-like activity 37.2-fold higher than natural laccase and 13.6-fold higher than a Cu^{II}_{3}–MOF analogue, while maintaining stability across pH 4–12 and achieving a 16.2-fold reduction in production cost. DFT calculations attribute the activity enhancement to Cu^{+} incorporation, which optimizes the electronic structure, lowers reaction barriers, and strengthens intermediate binding relative to the Cu^{II}_{3}–MOF. The material enables efficient degradation of phenolic pollutants, colorimetric discrimination of 11 phenols, and sensitive detection of epinephrine (LOD 6.5 μM) and dopamine (LOD 10 μM). Collectively, these results establish laccase-inspired MOF nanozymes as high-activity, low-cost, and durable platforms for environmental remediation and biosensing.

Acknowledgements

This work was supported by the National Natural Science Foundation of China (32501183), Applied Basic Research Foundation of Liaoning Province, China (2025JH2/101330098), Shandong Provincial Natural Science Foundation, China (No. ZR2024ME072, No. ZR2021QB163), Research Fund for Lin He's Academician Workstation of New Medicine and Clinical Translation in Jining Medical University (JYHL2022MS11).

Conflicts of Interest

The authors declare no conflicts of interest.

Data Availability Statement

The data that support the findings of this study are available from the corresponding author upon reasonable request.

References

1. E. Salvadeo, L. Dubois, and J.-M. Latour, "Trinuclear Copper Complexes as Biological Mimics: Ligand Designs and Reactivities," *Coordination Chemistry Reviews* 374 (2018): 345–375.

2. A. M. Geer, C. Musgrave Iii, C. Webber, et al., "Electrocatalytic Water Oxidation by a Trinuclear Copper(II) Complex," *ACS Catalysis* 11, no. 12 (2021): 7223–7240.

3. W. Zhang, C. E. Moore, and S. Zhang, "Multiple Proton-Coupled Electron Transfers at a Tricopper Cluster: Modeling the Reductive Regeneration Process in Multicopper Oxidases," *Journal of the American Chemical Society* 144, no. 4 (2022): 1709–1717.

4. G. C. Sedenho, R. N. P. Colombo, and F. N. Crespilho, "Insights from Enzymatic Catalysis: A Path Towards Bioinspired High-Performance Electrocatalysts," *ChemCatChem* 15, no. 15 (2023): 202300491.

5. J. Sheng, Y. Wu, H. Ding, et al., "Multienzyme-Like nanozymes: Regulation, Rational Design, and Application," *Advanced Materials* 36, no. 10 (2024): 2211210.

6. Y. Lu, C. Cao, X. Pan, Y. Liu, and D. Cui, "Structure Design Mechanisms and Inflammatory Disease Applications of Nanozymes," *Nanoscale* 15, no. 1 (2023): 14–40.

7. Y. Xu, Z. Zhou, N. Deng, et al., "Molecular Insights of Nanozymes From Design to Catalytic Mechanism," *Science China Chemistry* 66, no. 5 (2023): 1318–1335.

8. Z. Chen, Y. Yu, Y. Gao, and Z. Zhu, "Rational Design Strategies for Nanozymes," *ACS Nano* 17, no. 14 (2023): 13062–13080.

9. W.-D. Wang and Z.-J. Sun, "Evoking Pyroptosis with Nanomaterials for Cancer Immunotherapy: Current Boom and Novel Outlook," *Nano TransMed* 1, no. 1 (2022): 9130001.

10. Q. Ye and Y. S. Zhang, "The Era of Translational Nanomedicine," *Nano TransMed* 1, no. 1 (2022): 9130006.

11. Q.-F. Chen, Z.-Y. Cheng, R.-Z. Liao, and M.-T. Zhang, "Bioinspired Trinuclear Copper Catalyst for Water Oxidation with a Turnover Frequency up to 20000 s^{-1}," *Journal of the American Chemical Society* 143, no. 47 (2021): 19761–19768.

12. B. Kim and K. D. Karlin, "Ligand–Copper(I) Primary O_2-Adducts: Design, Characterization, and Biological Significance of Cupric–Superoxides," *Accounts of Chemical Research* 56, no. 16 (2023): 2197–2212.

13. M. Gil-Sepulcre, P. Garrido-Barros, J. Oldengott, et al., "Consecutive Ligand-Based Electron Transfer in New Molecular Copper-Based Water Oxidation Catalysts," *Angewandte Chemie International Edition* 60, no. 34 (2021): 18639–18644.

14. J. A. R. Navarro and B. Lippert, "Simple 1:1 and 1:2 Complexes of Metal Ions with Heterocycles as Building Blocks for Discrete Molecular as well as Polymeric Assemblies," *Coordination Chemistry Reviews* 222, no. 1 (2001): 219–250.

15. J. Wang, R. Huang, W. Qi, R. Su, B. P. Binks, and Z. He, "Construction of a Bioinspired Laccase-Mimicking Nanozyme for the Degradation and Detection of Phenolic Pollutants," *Applied Catalysis B: Environment and Energy* 254 (2019): 452–462.

16. H. Liang, F. Lin, Z. Zhang, et al., "Multicopper Laccase Mimicking Nanozymes with Nucleotides as Ligands," *ACS Applied Materials & Interfaces* 9, no. 2 (2017): 1352–1360.

17. S. S. Mohammed Ameen, A. Bedair, M. Hamed, F. R. Mansour, and K. M. Omer, "Recent Advances in Metal–Organic Frameworks as Oxidase Mimics: A Comprehensive Review on Rational Design and Modification for Enhanced Sensing Applications," *ACS Applied Materials & Interfaces* 17, no. 1 (2025): 110–129.

18. S. Zhang, H. Li, Q. Xia, D. Yang, and Y. Yang, "Zirconium-Porphyrin-MOF-Based Oxidase-Like Nanozyme with Oxygen Vacancy for Aflatoxin B1 Colorimetric Sensing," *Journal of Food Science* 89, no. 6 (2024): 3618–3628.

19. L. Zhao, D. Si, Y. Zhao, et al., "Copper nanocomposite Decorated Two-Dimensional Metal Organic Frameworks of Metalloporphyrin with Peroxidase-Mimicking Activity," *Colloids and Surfaces A: Physicochemical and Engineering Aspects* 644 (2022): 128876.

20. M. Wen, W.-Y. Yang, and Z.-P. Zhao, "Advancements in Nanoscale MOFs-Based Catalytic Materials: Synthesis Strategies and Applications," *Journal of Environmental Chemical Engineering* 13, no. 2 (2025): 115613.

21. D. Thakur, S. A. M. Sushmita, and A. K. Verma, "Advancement in Synthetic Strategies of Phosphorus Heterocycles: Recent Progress from Synthesis to Emerging Class of Optoelectronic Materials," *The Chemical Record* 24, no. 8 (2024): 202400058.

22. H. Rong, S. Ji, J. Zhang, D. Wang, and Y. Li, "Synthetic Strategies of Supported Atomic Clusters for Heterogeneous Catalysis," *Nature Communications* 11, no. 1 (2020): 5884.

23. Y. Yao, X. Zhao, G. Chang, X. Yang, and B. Chen, "Hierarchically Porous Metal–Organic Frameworks: Synthetic Strategies and Applications," *Small Structures* 4, no. 1 (2023): 2200187.

24. Y. Lu, X. Zhang, and Y. Huang, "Dual-Site Se/NC Specific Peroxidase-Like Nanozyme for Highly Sensitive Methimazole Detection," *Chinese Chemical Letters* 36, no. 4 (2025): 110129.

25. Y.-S. Wei, M. Zhang, R. Zou, and Q. Xu, "Metal–Organic Framework-Based Catalysts with Single Metal Sites," *Chemical Reviews* 120, no. 21 (2020): 12089–12174.

26. J. A. Brant, Y. Liu, D. F. Sava, D. Beauchamp, and M. Eddaoudi, "Single-Metal-Ion-Based Molecular Building Blocks (MBBs) Approach to the Design and Synthesis of Metal–Organic Assemblies," *Journal of Molecular Structure* 796, no. 1 (2006): 160–164.

27. S. T. Frey, H. H. J. Sun, N. N. Murthy, and K. D. Karlin, "A New Trinuclear Copper Complex and its Reactions with Plasmid DNA," *Inorganica Chimica Acta* 242, no. 1 (1996): 329–338.

28. J. Tang and L. Zhao, "Polynuclear Organometallic Clusters: Synthesis, Structure, and Reactivity Studies," *Chemical Communications* 56, no. 13 (2020): 1915–1925.

29. Q. Wang, R. P. Murphy, M. R. Gau, P. J. Carroll, and N. C. Tomson, "Controlling the Size of Molecular Copper Clusters Supported by a Multinucleating Macrocycle," *Inorganic Chemistry* 63, no. 39 (2024): 18332–18344.

30. J. Troyano, F. Zamora, and S. Delgado, "Copper(I)–Iodide Cluster Structures as Functional and Processable Platform Materials," *Chemical Society Reviews* 50, no. 7 (2021): 4606–4628.

31. W.-L. Duan, Y.-X. Li, Y. Feng, W.-Z. Li, and J. Luan, "Controllable Synthesis of Copper-Organic Frameworks via Ligand Adjustment for Enhanced Photo-Fenton-Like Catalysis," *Journal of Colloid and Interface Science* 646 (2023): 107–117.

32. S. Zhang and L. Zhao, "Macrocycle-encircled polynuclear Metal Clusters: Controllable Synthesis, Reactivity Studies, and Applications," *Accounts of Chemical Research* 51, no. 10 (2018): 2535–2545.

33. X. Chen, Z.-T. Chen, F. Zhu, et al., "Enhanced Organic Dye Adsorption and Photocatalytic Activity Through a Metal–Organic Framework Featuring Heptanuclear/Binuclear Clusters and Cage Cavities," *CrystEngComm* 26, no. 33 (2024): 4489–4497.

34. J. D. Schneider, B. A. Smith, G. A. Williams, et al., "Synthesis and Characterization of Cu(II) and Mixed-Valence Cu(I)Cu(II) Clusters Supported by Pyridylamide Ligands," *Inorganic Chemistry* 59, no. 8 (2020): 5433–5446.

35. E. I. Solomon, U. M. Sundaram, and T. E. Machonkin, "Multicopper Oxidases and Oxygenases," *Chemical Reviews* 96, no. 7 (1996): 2563–2606.

36. E. I. Solomon, D. E. Heppner, E. M. Johnston, et al., "Copper Active Sites in Biology," *Chemical Reviews* 114 (2014): 3659–3853.

37. A. Messerschmidt, R. Ladenstein, R. Huber, et al., "Refined Crystal Structure of Ascorbate Oxidase at 1.9 Å Resolution," *Journal of Molecular Biology* 224, no. 1 (1992): 179–205.

38. A. Messerschmidt, H. Luecke, and R. Huber, "X-Ray Structures and Mechanistic Implications of Three Functional Derivatives of Ascorbate Oxidase from Zucchini: Reduced, Peroxide and Azide Forms," *Journal of Molecular Biology* 230, no. 3 (1993): 997–1014.

39. L. Rulíšek and U. Ryde, "Theoretical Studies of the Active-Site Structure, Spectroscopic and Thermodynamic Properties, and Reaction Mechanism of Multicopper Oxidases," *Coordination Chemistry Reviews* 257, no. 2 (2013): 445–458.

40. K. Yu, M. Li, H. Chai, et al., "Mof-818 nanozyme-Based Colorimetric and Electrochemical Dual-Mode Smartphone Sensing Platform for In Situ Detection of H_2O_2 and H_2S Released From Living Cells," *The Chemical Engineering Journal* 451 (2023): 138321.

41. Y. Wang, C. He, W. Li, J. Zhang, and Y. Fu, "Catalytic Performance of Oligonucleotide-Templated pt Nanozyme Evaluated by Laccase Substrates," *Catalysis Letters* 147, no. 8 (2017): 2144–2152.

42. J. Wang, R. Huang, W. Qi, R. Su, and Z. He, "Oriented Enzyme Immobilization at the Oil/Water Interface Enhances Catalytic Activity and Recyclability in a Pickering Emulsion," *Langmuir* 33, no. 43 (2017): 12317–12325.

43. M. Lu, A. Dong, X. Li, et al., "The Synthesis of Cu-TCPP MOF/g-C_3N_4 Heterojunctions as Efficient Photocatalysts for Hydrogen Generation," *New Journal of Chemistry* 47, no. 44 (2023): 20336–20343.

44. L. Wang, S.-R. Li, Y.-Z. Chen, and H.-L. Jiang, "Encapsulating Copper Nanocrystals into Metal–Organic Frameworks for Cascade Reactions by Photothermal Catalysis," *Small* 17, no. 22 (2021): 2004481.

45. G. Zheng, Z. Xing, X. Gao, C. Nie, Z. Xu, and Z. Ju, "Fabrication of 2D Cu-BDC MOF and its Derived Porous Carbon as Anode Material for High-Performance Li/K-Ion Batteries," *Applied Surface Science* 559 (2021): 149701.

46. X. Wu, C. Cai, Q. Cen, et al., "Efficient Catalytic Removal of Phenolic Pollutants by Laccase From Coriolopsis Gallica: Binding interaction and polymerization mechanism," *International Journal of Biological Macromolecules* 279 (2024): 135272.

47. P. Zhang, J. Xu, X. Zhang, C. Hou, and D. Wu, "Catalytic Removal of Emerging Contaminants and Phenolic Compounds by Laccase: Transformation Mechanisms in Aquatic Environments—Polymerization Or Degradation?," *Separation and Purification Technology* 355 (2025): 129544.

48. Y. Yang, Y. Wang, Q. Huang, et al., "Enhancing the Catalytic Activity of Laccase@Copper–Metal–Organic Framework Nanofractal Microspheres: Synergistic Contribution of the Mass Transfer and Electron Transfer Pathway," *Inorganic Chemistry* 63, no. 24 (2024): 11325–11339.

Supporting Information

Additional supporting information can be found online in the Supporting Information section.

Supporting file: smtd70454-sup-0001-SuppMat.docx.